

Article

Solid-state ball milling synthesis of high-capacity multiphase nanoscale Bi/Co₄S₃-C as an anode material for lithium-ion batteries

Liwen Zhang¹, Ting Yue¹, Yihong Ding^{1,*}, Huilei Jin¹, Tianbiao Zeng^{1,2,*}¹ Wenzhou Key Lab of Advanced Energy Storage and Conversion, Zhejiang Province Key Lab of Leather Engineering, College of Chemistry and Materials Engineering, Wenzhou University, Wenzhou 325035, China² Research Institute of Interdisciplinary Sciences (RISE) and School of Materials Science & Engineering, Dongguan University of Technology, Dongguan 523808, China

* Corresponding authors: Yihong Ding, 20195205@wzu.edu.cn; Tianbiao Zeng, tianbiaoZeng@126.com

CITATION

Zhang L, Yue T, Ding Y, et al. Solid-state ball milling synthesis of high-capacity multiphase nanoscale Bi/Co₄S₃-C as an anode material for lithium-ion batteries. *Characterization and Application of Nanomaterials*. 2025; 8(2): 11620. <https://doi.org/10.24294/can11620>

ARTICLE INFO

Received: 21 March 2025

Accepted: 28 April 2025

Available online: 29 May 2025

COPYRIGHT



Copyright © 2025 by author(s). *Characterization and Application of Nanomaterials* is published by EnPress Publisher, LLC. This work is licensed under the Creative Commons Attribution (CC BY) license. <https://creativecommons.org/licenses/by/4.0/>

Abstract: Cobalt-based sulfides have emerged as promising candidates for next-generation high-performance anode materials for lithium-ion batteries (LIBs) due to their high theoretical specific capacity and reversible conversion reaction mechanisms. However, their practical application is hindered by volume expansion effects and relatively low rate performance. Guided by theoretical principles, this study synthesizes nanoscale Bi/CoS-C and Bi/Co₄S₃-C (denoted as Bi/CS-C) composite materials using Co and Bi₂S₃ as precursors via a solid-state ball milling method. The electrochemical properties of these materials were systematically investigated. When employed as anodes for LIBs, Bi/CoS-C and Bi/CS-C exhibit excellent rate capabilities. At current densities of 0.1, 0.5, 1, 4, and 10 A/g, the reversible capacities of Bi/CoS-C were 939.2, 730.7, 655.6, 508.1, and 319 mAh/g, respectively. In contrast, Bi/CS-C exhibited reversible capacities of 760.4, 637.6, 591.9, 484.3, and 295.4 mAh/g, respectively. Moreover, Co₄S₃, as an active component, enables superior long-cycle performance compared to CoS. After 300 cycles at 0.2 A/g, the Bi/CoS-C and Bi/CS-C electrodes retained capacities of 193.1 and 788.8 mAh/g, respectively. This study demonstrates that nanostructure design and carbon-based composite materials can effectively mitigate the volume expansion issue of cobalt-based sulfides, thereby enhancing their rate performance and cycling stability. This strategy provides new insights for the development of high-performance anode materials for lithium-ion batteries and is expected to accelerate their practical application in next-generation energy storage devices.

Keywords: lithium-ion batteries; anode materials; nanoparticles; Bi/CoS-C; Bi/Co₄S₃-C

1. Introduction

With the rapid development of renewable energy technologies, LIBs have become the key energy storage devices for electric vehicles, portable electronic devices, and large-scale energy storage systems due to their high energy density, long cycle life, and environmental friendliness [1–3]. However, the theoretical specific capacity of conventional graphite anode materials is only 372 mAh/g. Their relatively low specific capacity and rate performance fail to meet the demands of next-generation high-performance energy storage devices for high energy density, high power density, and long cycle life [4,5]. Therefore, the development of novel anode materials with higher specific capacity, superior rate performance, and enhanced cycling stability has become a key research focus [6]. Among various emerging anode materials, transition metal sulfides (TMSs) are considered one of the most promising candidates due to their reversible conversion reaction mechanisms

and high theoretical specific capacity [7–9]. In particular, cobalt-based sulfides (Co_xS_y) have attracted significant attention in LIB anode material research due to their high electronic conductivity, excellent lithium-ion diffusion kinetics, and appropriate electrochemical reaction potential [10,11]. However, pure Co_xS_y undergoes significant volume expansion during charge/discharge cycles, leading to electrode structural degradation, poor rate performance, and rapid capacity fading, which severely limit its practical application.

To address these challenges, researchers have proposed various strategies to mitigate the volume expansion of Co_xS_y and enhance its lithium storage performance, including: (1) Rationally designed composite structures, incorporating other metals or constructing multiphase TMS composite materials to form stable heterostructures [12,13]; (2) nanostructuring electrode materials, reducing particle size to increase specific surface area and accelerate lithium-ion diffusion kinetics [14–16]; (3) incorporating carbon-based materials (e.g., porous carbon, graphene, and its derivatives) to construct conductive networks and buffer volume expansion, thereby improving cycling stability [17,18]. Notably, the introduction of carbon-based materials plays a crucial role in enhancing the electrochemical performance of Co_xS_y anode materials, with key advantages in three aspects: (I) Excellent interfacial regulation, effectively encapsulating Co_xS_y particles and enhancing their structural stability; (II) superior electrical conductivity and mechanical strength, facilitating fast electron/ion transport and alleviating volume expansion; (III) a highly porous structure and large specific surface area (typically $> 1000 \text{ m}^2/\text{g}$), increasing the electrode-electrolyte contact area and providing more active sites for Li^+ storage.

Recent studies have highlighted the potential of bismuth (Bi) and its compounds as promising anode materials for lithium-ion batteries, owing to their high theoretical capacity (385 mAh/g for Bi) and a distinctive alloying/dealloying mechanism that enables fast kinetics and reversible lithium storage [19,20]. Furthermore, compared with other alloy-type anode materials, Bi exhibits a relatively low volume expansion ($\sim 220\%$), which helps mitigate structural degradation. When Bi is composited with cobalt-based sulfides, it can regulate internal stress and suppress local phase transitions during cycling. Notably, Yu et al. synthesized Co_4S_3 nanoparticles embedded in a carbon-based interface using a phase-inversion strategy that integrates in situ sulfidation and carbonization [21]. This material significantly enhanced interfacial selectivity and maintained a specific capacity of 563.5 mAh/g after 400 cycles at 4.0 C. In addition, Jiang et al. developed an environmentally friendly in situ method to fabricate nitrogen-doped $\text{Co}_9\text{S}_8/\text{Co}_4\text{S}_3$ nanoparticles coated with carbon and anchored onto reduced graphene oxide sheets (N-CS@C/G) [10]. In this composite, Co_4S_3 provides additional electrochemically active sites for lithium storage, enabling the N-CS@C/G electrode to exhibit progressive cycling stability with a capacity of 662 mAh/g at 2 A/g. These findings underscore the remarkable advantages of Bi-based and Co_4S_3 -containing composites in enhancing the structural stability and electrochemical performance of lithium-ion battery anodes, especially when synergistically integrated with conductive carbon frameworks.

Based on these insights, this study selected Co and Bi_2S_3 as precursors to synthesize Bi/CoS and Bi/ Co_4S_3 composite materials via a solid-state reaction. These

materials were then anchored onto exfoliated graphite through ball milling, forming nanoscale heterostructured Bi/CoS-C and Bi/Co₄S₃-C (Bi/CS-C) composites. Among them, the Bi/CS-C composite exhibited the most significant synergistic enhancement, with key advantages in the following aspects: (1) The introduction of Bi, through the formation of a nanocomposite structure with Co₄S₃, plays a role in modulating internal stress and mitigating local structural distortions. This contributes to enhanced structural stability of the electrode material during charge-discharge cycles and helps suppress structural degradation caused by the volume changes of Co₄S₃ [19,22]; (2) the synergistic effect of carbon-based materials further enhanced the electronic conductivity and rate performance of the material, accelerated Li⁺ diffusion kinetics, and alleviated mechanical stress during charge/discharge cycles through the flexible carbon framework; (3) the optimized nanostructure provided a larger specific surface area and more active sites, enhancing electrode-electrolyte interactions, improving Li⁺ storage capacity, and increasing interfacial stability. Experimental results demonstrated that nanostructure design and carbon-based material incorporation effectively mitigated the volume expansion of cobalt-based sulfides, significantly enhancing their rate performance and cycling stability. This strategy offers new insights for the development of high-performance anode materials for LIBs.

2. Materials and methods

2.1. Synthesis of Bi/Co_{1-x}S-C and Bi/Co₄S₃-C materials

Cobalt powder (Co), graphite (C), and bismuth sulfide (Bi₂S₃) were purchased from Shanghai Macklin Biochemical Co., Ltd. All chemicals were used as received without further purification. First, Co and Bi₂S₃ were mixed in molar ratios of 1:1, 2:1, 3:1, and 4:1 and ground in an agate mortar until no visible particles remained. The mixtures were then loaded into a quartz tube, vacuum-sealed, and placed in a tube furnace. The temperature was increased at a rate of 5 °C/min and maintained at 600 °C for 6 h. After the reaction, the obtained samples were cooled to room temperature and ground into fine powders using an agate mortar, yielding four different products. Based on X-ray diffraction (XRD) analysis, the Bi/CoS and Bi/Co₄S₃ (Bi/CS) products obtained from the 3:1 and 4:1 molar ratios were selected and mixed with 15 wt.% graphite. The mixtures were then subjected to ball milling at a rotational speed of 900 r/min under a nitrogen atmosphere for 10 h to obtain the Bi/CoS-C and Bi/Co₄S₃-C (Bi/CS-C) composites.

2.2. Material characterization

The crystallographic information of the samples was studied using an X-ray diffractometer (XRD, Shimadzu-XRD-7000S, Cu K α , 40 kV, 40 mA) with a scan range of 10°–80° and a step size of 0.02°. The morphology and microstructure of the prepared samples were characterized using a scanning electron microscope (SEM, Nova 200 NanoSEM) and a high-resolution transmission electron microscope (TEM, JEM-2100F).

2.3. Electrode preparation and electrochemical performance evaluation

The active material, acetylene black, and carboxymethyl cellulose sodium salt were mixed in a mass ratio of 8:1:1 and stirred with an appropriate amount of deionized water for 2 h to form a slurry. The slurry was then uniformly coated onto copper foil using a 50 μm film applicator and dried in a vacuum oven at 60 $^{\circ}\text{C}$ for 2 h. The coated copper foil was punched to form disks with a diameter of 12 mm, which were used as anodes. The sample mass on each electrode was 1.5 ± 0.1 mg/cm^2 . The CR2032 coin cells were assembled in an argon-filled glove box, where the levels of water and oxygen in the glove box were both below 0.1 ppm. The electrolyte was 1 mol/L LiPF_6 dissolved in a mixture of ethylene carbonate (EC), dimethyl carbonate (DMC), and ethyl methyl carbonate (EMC) in a volume ratio of 1:1:1 (vol%), with 5.0% fluoroethylene carbonate (FEC). The separator used for the LIBs was a porous polypropylene membrane (Celgard-2300). The assembled LIBs were tested for charge/discharge, Galvanostatic Intermittent Titration Technique (GITT), and rate performance using a LAND battery tester. Cyclic voltammetry (CV) tests were conducted using an EC-100B electrochemical workstation.

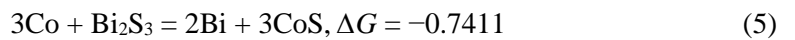
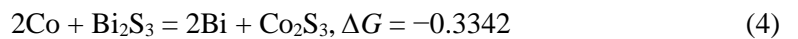
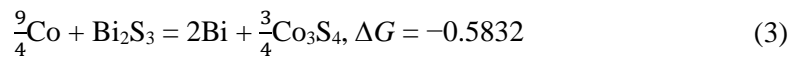
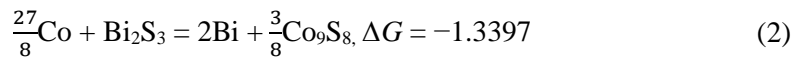
3. Results and discussion

3.1. Theory

The equations for the Co and Bi_2S_3 system were written based on the final energy/atom values of each crystal from the Materials Project website, and the calculation of the Gibbs free energy ΔG of the reactions is given by Equation (1) [23,24]:

$$\Delta G = G_{\text{products}} - G_{\text{reactants}} \quad (1)$$

where G_{products} and $G_{\text{reactants}}$ represent the Gibbs free energies of the products and reactants, respectively. The changes in ΔG for a series of predicted chemical reactions are shown in Equations (2)–(5) below:



From the above calculation results, it is evident that all the ΔG values are negative, indicating that these reactions are thermodynamically feasible. Next, the Gibbs free energy for each mole of Co was normalized, with the formula $\Delta G/n$, where n is the coefficient of Co in the chemical equation. The $\Delta G/n$ values for reactions (2)–(5) are -0.3969 , -0.2592 , -0.1671 , and -0.2740 eV, respectively. Thus, it can be concluded that the driving force for the reaction of Co with Bi_2S_3 to form Co_9S_8 is the greatest, followed by the formation of CoS, Co_3S_4 , and Co_2S_3 . Therefore, to systematically study the effect of the Co/ Bi_2S_3 molar ratio on the reaction products and further explore the formation patterns of possible cobalt

sulfide phases, this study chose Co:Bi₂S₃ molar ratios of 1:1, 2:1, 3:1, and 4:1 for solid-state reactions to cover the above reaction systems.

3.2. Characterization

After performing solid-state reactions with Co:Bi₂S₃ molar ratios of 1:1, 2:1, 3:1, and 4:1, the obtained products were characterized by X-ray diffraction (XRD), and their diffraction patterns are shown in **Figure 1a–c**. As observed in the figure, for molar ratios of 1:1 and 2:1, diffraction peaks corresponding to Bi were detected in the reaction products, indicating that Bi₂S₃ was partially reduced. However, residual Bi₂S₃ was still present, suggesting that the reaction was incomplete. In contrast, at molar ratios of 3:1 and 4:1, Bi₂S₃ was fully converted, forming Bi/Co_{1-x}S and Bi/Co₄S₃ (Bi/CS) composite materials, respectively. This indicates that a higher Co/Bi₂S₃ ratio facilitates complete reaction and the formation of a stable cobalt sulfide phase. The value of x was determined using Equation (6):

$$C = n \times F / [3.6 \times (M_{\text{Bi}_2\text{S}_3} + M_{\text{Co}}y)] \quad (6)$$

where F is the Faraday constant ($F = 96485.6$ C/mol, given that $1 \text{ eV} = 96485.6$ J/mol), $n = 12$ represents the total number of electrons transferred per mole of Bi₂S₃ during Li⁺ storage, and 3.6 is the conversion factor between coulombs and milliampere-hours. $M_{\text{Bi}_2\text{S}_3}$ and M_{Co} represent the molar masses of Bi₂S₃ and Co, respectively, and y is the Co/Bi₂S₃ molar ratio. Based on the calculations, when the Co:Bi₂S₃ molar ratio is 3:1, the target materials are CoS and Bi, yielding $x = 0$. Additionally, Chen et al. conducted XRD characterization of CoS@C, and the XRD patterns of Co_{1-x}S synthesized in this study closely matched their results [25]. This confirms that the synthesized Bi/Co_{1-x}S theoretically corresponds to the predicted Bi/CoS composite material [26,27]. Since residual unreacted Bi₂S₃ was still present in the 1:1 and 2:1 reaction systems, they were not further investigated.

To further explore the optimal molar ratio for the reaction between Co and Bi₂S₃, the Bi/CoS and Bi/CS materials synthesized at 3:1 and 4:1 molar ratios were ball-milled with 15 wt.% graphite, yielding Bi/CoS-C and Bi/CS-C, respectively, as shown in **Figure 1b,c**. Notably, no XRD peaks corresponding to graphite were observed in the Bi/CoS-C and Bi/CS-C composite materials, suggesting that the graphite may have been partially or completely transformed into an amorphous disordered structure during the ball-milling process. Moreover, compared to Bi/CoS and Bi/CS, the peak intensities of Bi/CoS-C and Bi/CS-C were significantly reduced. This is primarily attributed to the high-energy mechanical forces applied during the ball-milling process, which induce a certain degree of disorder in the Bi/CoS and Bi/CS active materials, thereby affecting their crystalline structure and XRD diffraction characteristics. Meanwhile, the exfoliated graphite, serving as a conductive framework, is uniformly distributed throughout the composite system and contributes to structural stabilization, although it is not the main cause of the observed crystallographic disorder. Furthermore, as shown in the Raman spectra in **Figure 1d**, two prominent characteristic peaks are clearly observed at approximately 1350 cm^{-1} (D band) and 1580 cm^{-1} (G band) in the Bi/Co₄S₃-C and Bi/CoS-C samples. These peaks correspond to disordered carbon (D band) and graphitic carbon

(G band), which are typical Raman features of carbon-based materials. In contrast, the Bi/Co₄S₃ and Bi/CoS samples without carbon composites exhibit negligible Raman signals in the same wavenumber range, indicating the absence of carbon components in these materials.

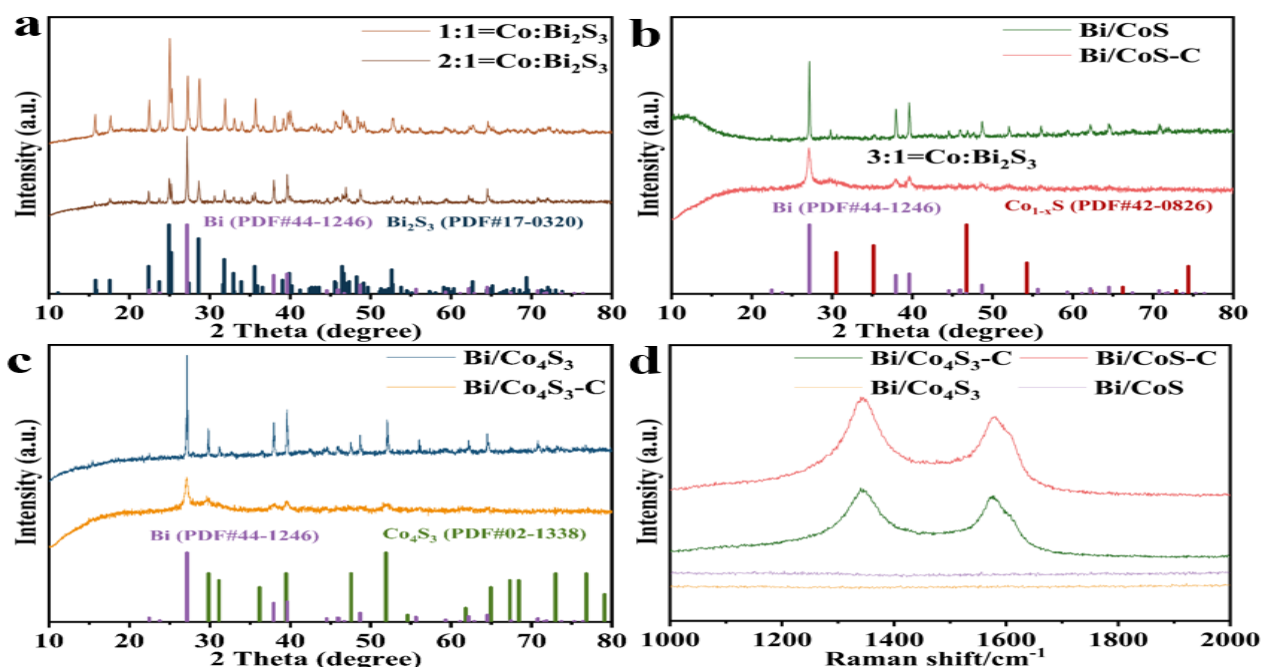


Figure 1. (a) XRD patterns of samples with Co:Bi₂S₃ molar ratios of 1:1 and 2:1; (b) XRD patterns of Bi/Co_{1-x}S and Bi/Co_{1-x}S-C composites (Co:Bi₂S₃ = 3:1); (c) XRD patterns of Bi/Co₄S₃ and Bi/Co₄S₃-C composites (Co:Bi₂S₃ = 4:1); (d) Raman patterns of Bi/Co₄S₃, Bi/Co₄S₃-C, Bi/CoS and Bi/CoS-C.

To analyze the effects of different molar ratios and ball milling treatment on the microstructure of the materials, SEM was used to examine the Bi/CoS, Bi/CoS-C, Bi/CS, and Bi/CS-C composites at a 20 μm scale. **Figure 2a,c** present the morphology of the Bi/CoS and Bi/CS composites, both of which exhibit large agglomerated structures with relatively rough surfaces. Notably, the Bi/CS composite shows a certain degree of interfacial distribution between particles, indicating good integration between different phases in the material. **Figure 2b,d** display the SEM images of the Bi/CoS-C and Bi/CS-C composites. Compared to Bi/CoS and Bi/CS, Bi/CoS-C and Bi/CS-C exhibit a more uniform and finer particle distribution. This suggests that the introduction of graphite during the ball milling process may have played a role in dispersion, preventing further particle agglomeration. Additionally, the overall reduction in particle size is likely attributed to the fragmentation effect induced by mechanical ball milling.

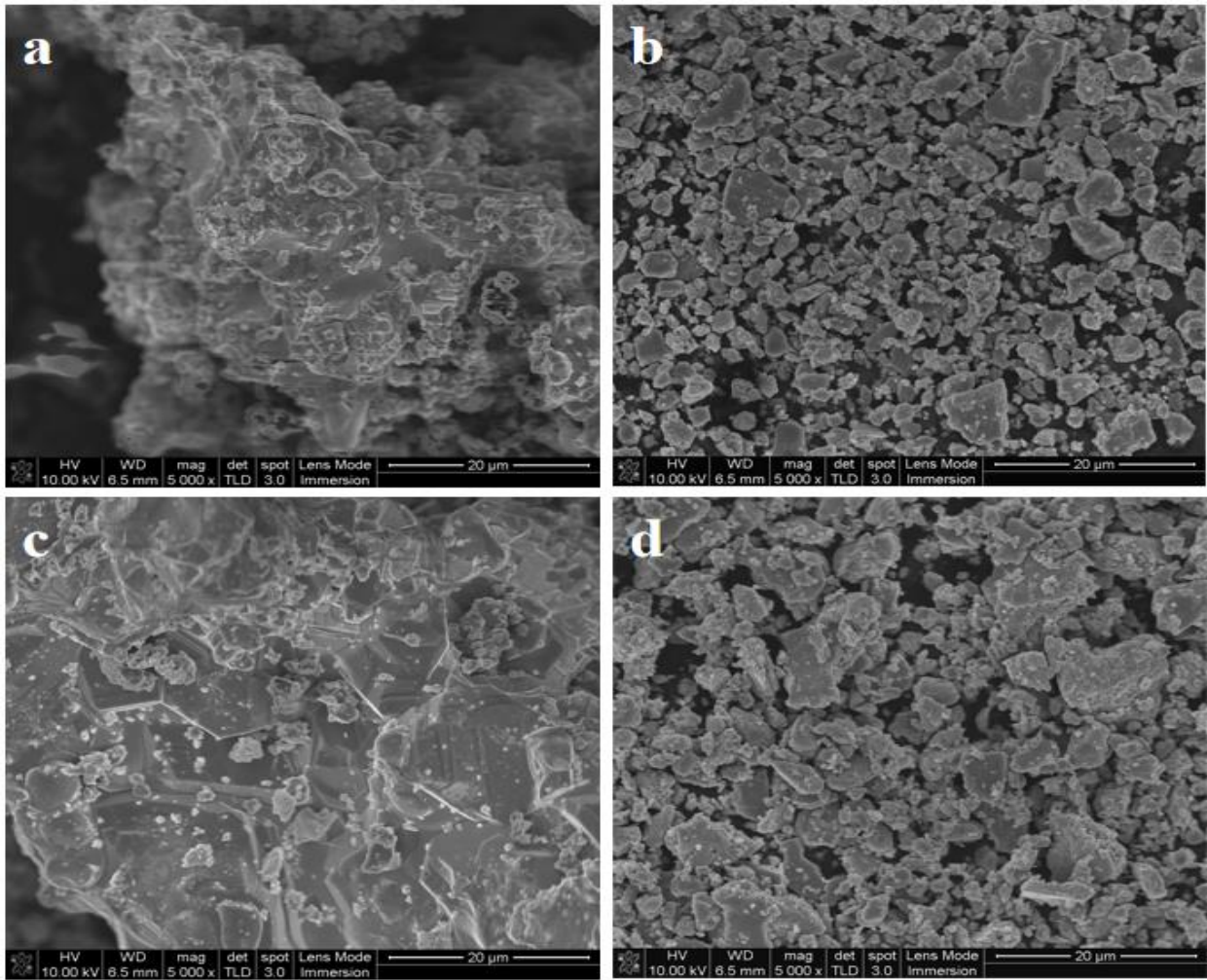


Figure 2. SEM images of (a) Bi/CoS; (b) Bi/CoS-C; (c) Bi/Co₄S₃; and (d) Bi/Co₄S₃-C composites at a 20 μm scale.

To further verify the regulatory effect of ball milling on the crystal structure of the materials, the crystallite sizes of the samples were calculated based on the characteristic diffraction peaks from the XRD patterns shown in **Figure 1b,c**, as summarized in **Table 1**. The crystallite sizes were calculated using the Scherrer Equation (7),

$$D = \frac{K\lambda}{\beta \cos\theta} \quad (7)$$

where D is the crystallite size, K is the shape factor (typically 0.9), λ is the X -ray wavelength (Cu $K\alpha$, 0.15406 nm), β is the full width at half maximum (FWHM) of the main XRD peak (in radians), and θ is the Bragg angle of the corresponding peak. The results indicate that, compared to the non-carbon-coated Bi/CoS and Bi/CS samples, the corresponding Bi/CoS-C and Bi/CS-C samples exhibit significantly broader diffraction peaks across multiple crystallographic planes. The FWHM values increased markedly, with the average crystallite sizes decreasing from 26.84 nm (Bi/CoS) and 54.05 nm (Bi/CS) to 12.14 nm (Bi/CoS-C) and 9.94 nm (Bi/CS-C), respectively. This further corroborates that the synergistic effect of ball milling significantly refines the particle size, thereby promoting the formation of more stable

electrochemical reaction interfaces and enhancing the exposure of additional active sites.

Table 1. FWHM values of XRD characteristic peaks and corresponding crystallite sizes of different samples calculated based on the Scherrer equation.

Sample	2θ (°)	FWHM (°)	B (rad)	$\cos(\theta)$	Crystallite Size (nm)
Bi/Co ₄ S ₃	27.17045	0.15469	0.0027	0.9719	52.25
	29.83264	0.14919	0.00261	0.9667	54.39
	39.6288	0.18724	0.00327	0.9424	44.56
	52.05749	0.1345	0.00235	0.8991	65.01
Average	-	-	-	-	54.05
Bi/Co ₄ S ₃ -C	27.11967	0.65054	0.01136	0.972	12.48
	29.95035	0.89421	0.01561	0.9664	9.02
	39.60183	0.73836	0.01289	0.9426	10.61
	51.96184	1.14691	0.02001	0.8994	7.65
Average	-	-	-	-	9.94
Bi/CoS	27.17189	0.29735	0.00519	0.9719	27.13
	37.9771	0.31609	0.00552	0.9478	26.43
	39.63194	0.31626	0.00552	0.9424	26.96
Average	-	-	-	-	26.84
Bi/CoS-C	27.13421	0.55814	0.00974	0.972	14.46
	37.9551	0.76598	0.01337	0.948	10.91
	39.60505	0.71549	0.01249	0.9426	11.04
Average	-	-	-	-	12.14

Figure 3 presents the TEM images of Bi/CoS-C and Bi/CS-C composites along with the corresponding energy-dispersive X-ray spectroscopy (EDS) elemental distribution analysis to further reveal the microscopic morphology and elemental distribution of the materials. **Figure 3a,b** show the TEM images of Bi/CoS-C and Bi/CS-C composites. Both materials exhibit a distinct nanoparticle aggregation structure, with the core region displaying a higher electron density, indicating the coexistence of Bi and CoS or Co₄S₃ particles. Furthermore, the peripheral region exhibits a lower electron density, which is presumed to correspond to the graphite distribution. This suggests that graphite may have uniformly coated the Bi/CoS-C and Bi/CS-C composite particles during the ball milling process. **Figure 3c,d** show the EDS elemental distribution maps of Bi/CoS-C and Bi/CS-C composites. The uniform distribution of Co, Bi, S, and C elements further confirms that Bi and CoS or Co₄S₃ are homogeneously dispersed and closely connected with exfoliated graphite at the nanoscale. The TEM and EDS results indicate that the ball milling process facilitates the uniform distribution of graphite within the Bi/CoS and Bi/CS composites. Additionally, distinct lattice fringes can be observed in the high-resolution TEM images, as shown in **Figure 4a,c**. In **Figure 4a**, the interplanar spacings are measured as 1.03 Å and 1.55 Å, corresponding to the (114) plane of CoS and the (107) plane of Bi, respectively. Similarly, in **Figure 4c**, the interplanar

spacings of Bi and Co_4S_3 are measured as 1.65 Å and 2.87 Å for the (024) and (222) lattice planes, respectively. These findings suggest that the nanoscale Bi_2S_3 particles are separated by Bi nanoparticles and that the nanosized Bi/CoS and Bi/CS particles are encapsulated within graphite layers. **Figure 4b,d** present the selected area electron diffraction (SAED) patterns of Bi/CoS-C and Bi/CS-C, showing distinct diffraction rings. This further confirms the coexistence of Bi and CoS or Co_4S_3 in the Bi/CoS-C and Bi/CS-C composites, indicating their well-defined polycrystalline nature.

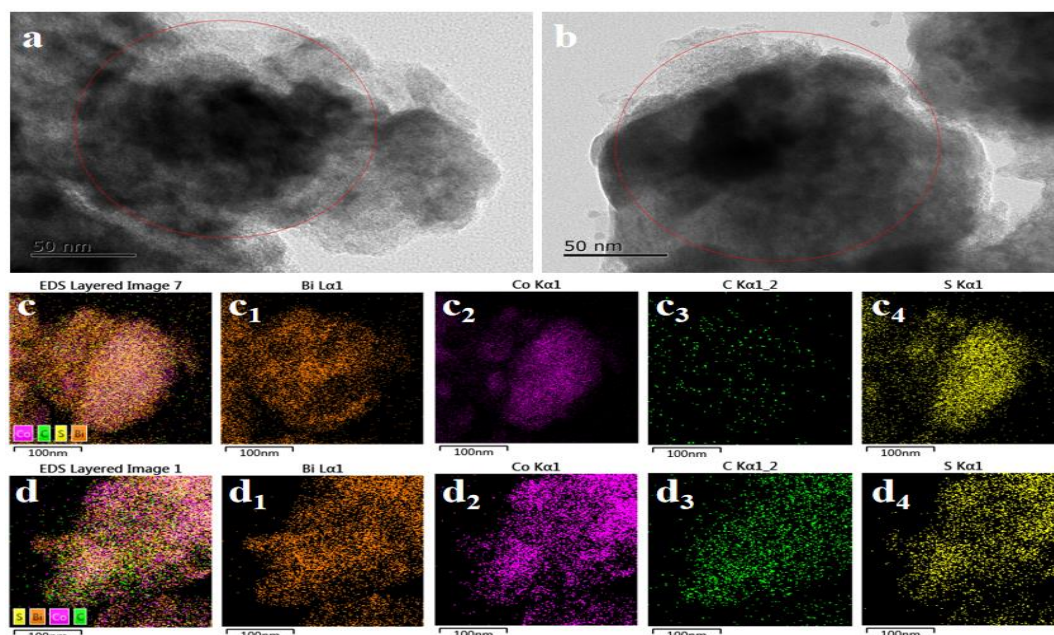


Figure 3. (a,b) TEM images of Bi/CoS-C and Bi/Co₄S₃-C; (c,c₁–c₄) Elemental distribution maps of Bi, Co, C, and S in Bi/CoS-C; (d,d₁–d₄) Elemental distribution maps of Bi, Co, C, and S in Bi/Co₄S₃-C.

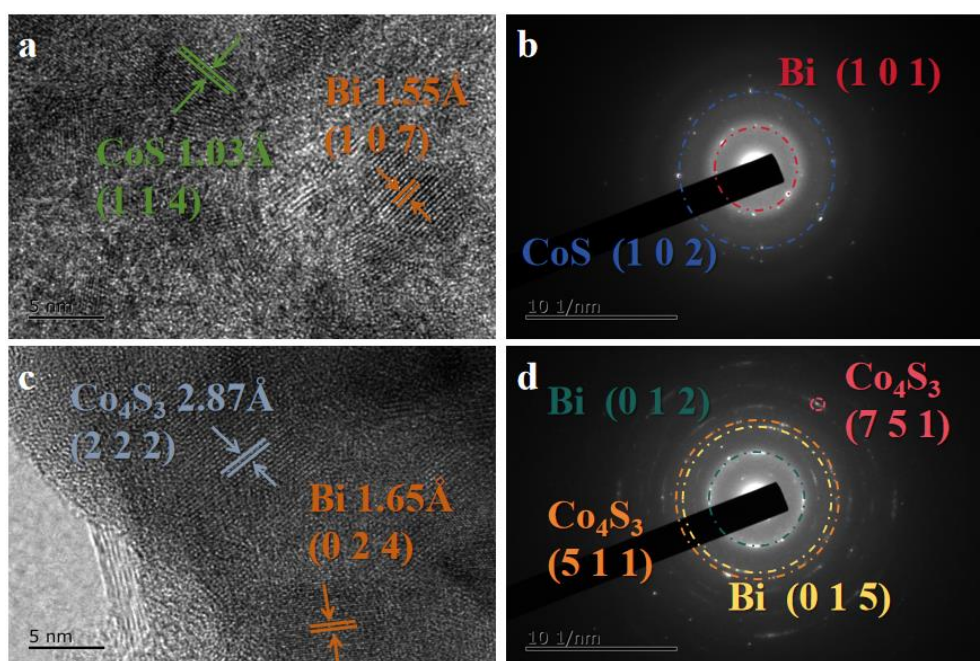
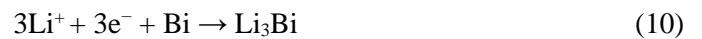


Figure 4. (a,b) TEM and SAED images of Bi/CoS-C; (c,d) TEM and SAED images of Bi/Co₄S₃-C.

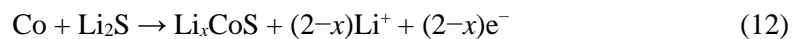
3.3. Testing

Based on this, to further investigate the lithium storage mechanisms of Bi/CoS, Bi/CS, Bi/CoS-C, and Bi/CS-C composites, cyclic voltammetry (CV) tests and differential charge/discharge curve (dQ/dV) analyses were conducted for each electrode material. The dQ/dV profiles of Bi/CoS and Bi/CS are shown in **Figure 5a,c**, respectively, while the CV curves of Bi/CoS-C and Bi/CS-C at a scan rate of 0.1 mV/s are presented in **Figure 5b,d**. During the initial cathodic scan, Bi/CoS and Bi/CS electrodes exhibit pronounced reduction peaks at 1.16 V and 1.11 V, respectively. In contrast, Bi/CoS-C and Bi/CS-C electrodes show similar irreversible current peaks at 0.63 V and 0.56 V, which can be primarily attributed to the formation of the solid electrolyte interphase (SEI) and the initial structural activation of the electrode materials during the first charge-discharge cycle. This process consumes a portion of lithium ions, leading to shifts in the position and intensity of current peaks in subsequent cycles. From the second to the fifth scan, the CV curves of the Bi/CoS-C and Bi/CS-C electrodes progressively overlap, indicating excellent electrochemical reversibility and cycling stability. As shown in **Figure 5b**, during the second to fifth scans of Bi/CoS-C, the reduction peak at 1.32–1.36 V is associated with Li⁺ insertion, forming Li_xCoS. A strong reduction peak at 0.75~0.78 V corresponds to the conversion reaction of Li_xCoS, leading to the formation of Co and Li₂S [28]. Subsequently, the reduction peak at 0.63–0.66 V corresponds to the alloying reaction of Bi, forming the Li₃Bi phase [25]. Additionally, the oxidation peaks at 0.88–0.90 V and 2.00–2.02 V correspond to the multi-step dealloying reaction of Li₃Bi and the reverse conversion reaction of Co, respectively. To gain deeper insight into the lithium storage mechanism, the above reactions can be described by the following Equations (8)–(13):

Discharge process:

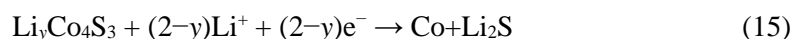
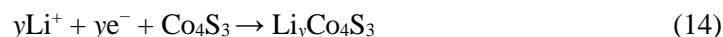


Charge process:



As shown in **Figure 5d**, after the first cycle activation, a significant reduction peak was observed at 1.29–1.32 V for the Bi/CS-C electrode. This is likely the initial reaction of Li⁺ insertion into the Co₄S₃ structure, forming Li_yCo₄S₃ (14) [17,29]. A new peak was detected at 0.77 V, corresponding to the conversion reaction of Li_yCo₄S₃, leading to the formation of Co and Li₂S (15) [10]. It is further speculated that the reduction peak at 0.61 V corresponds to the alloying reaction of Bi, forming Li₃Bi (16) [21,30,31]. During the anodic scan, the oxidation peak observed at 0.93–0.94 V is likely attributed to the delithiation reaction of Li₃Bi. The oxidation peak at

2.04–2.07 V likely represents the desorption process of Li_2S and Co, leading to the formation of $\text{Li}_y\text{Co}_4\text{S}_3$, as well as a more extensive reversible delithiation process, which essentially restores the Co_4S_3 active material to its initial state, completing a full cycle.



Based on this, the reaction sequence of Bi/CS-C composite with lithium should be $\text{Co}_4\text{S}_3 \rightarrow \text{Li}_y\text{Co}_4\text{S}_3 \rightarrow \text{Bi}$. It can be seen that both Bi/CS-C and Bi/CoS-C exhibit good electrochemical stability. However, Bi/CS-C, with its higher oxidation/reduction peak currents and broader potential range, may have superior performance in energy storage applications. This suggests that Co_4S_3 has a stronger synergistic effect on the electrochemical behavior of Bi compared to CoS.

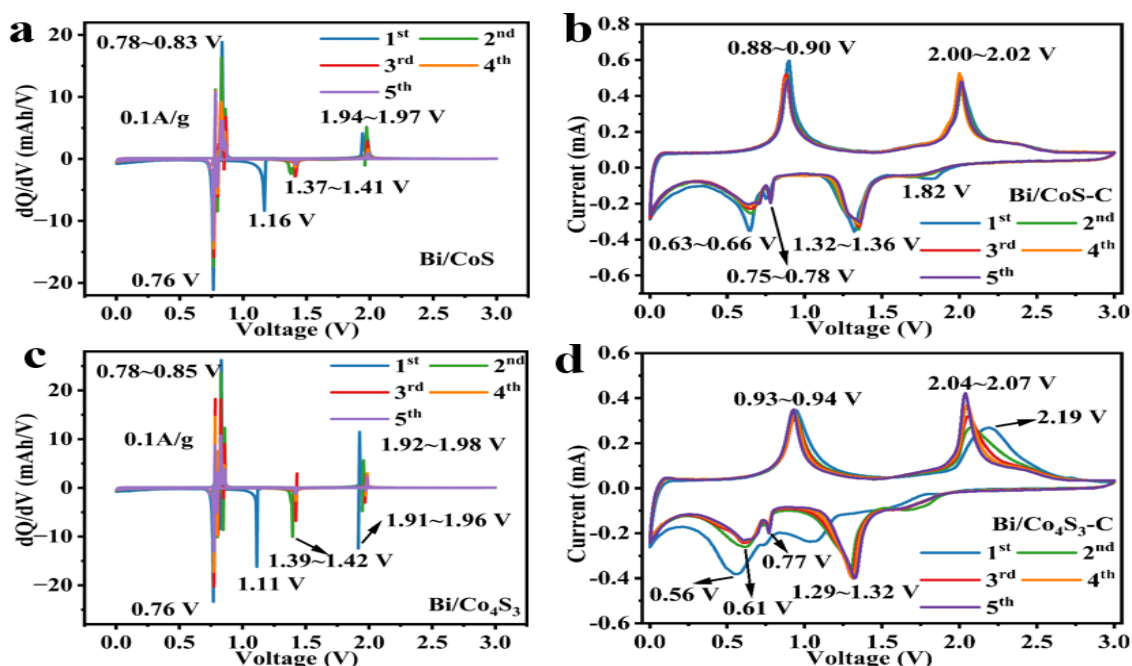


Figure 5. (a,c) Differential capacity curves (dQ/dV vs. V) of Bi/CoS and Bi/Co $_4$ S $_3$ electrodes at 0.1 A/g; (b,d) Cyclic voltammetry (CV) curves of Bi/CoS-C and Bi/Co $_4$ S $_3$ -C at a scan rate of 0.1 mV/s.

To further evaluate the electrochemical performance of Bi/CoS, Bi/CoS-C, Bi/CS, and Bi/CS-C electrodes during the charge-discharge process, the cycling performance of the materials was tested at a low current of 0.2 A/g, as shown in **Figure 6a**. The experimental results indicate that the initial specific capacities of the Bi/CoS-C and Bi/CS-C electrodes reached 959.7 mAh/g and 852.6 mAh/g, respectively, significantly outperforming the reversible capacities of Bi/CoS and Bi/CS electrodes at 647.4 mAh/g and 690.4 mAh/g. This suggests that the incorporation of carbon materials effectively enhances the lithium storage capacity of the electrode materials. However, during prolonged cycling, the specific capacity of Bi/CoS and Bi/CS electrodes showed a rapid decay trend. After 50 cycles, their

reversible capacities decreased to about 100 mAh/g, indicating poor structural stability and irreversible morphological or phase structure changes of the electrode materials during repeated charge-discharge cycles. In contrast, Bi/CoS-C and Bi/CS-C electrodes exhibited superior cycling stability, with the Bi/CS-C electrode maintaining a high reversible capacity of 788.8 mAh/g after 300 cycles, demonstrating excellent long-term stability. Although Bi/CoS-C has a higher initial specific capacity, its capacity begins to decay significantly after 150 cycles. This indicates that Co_4S_3 has better structural stability compared to CoS, which contributes to improving the cycling life of the electrode materials. The incorporation of carbon materials not only enhanced the specific capacity of Bi/CoS and Bi/CS electrodes but also effectively improved their cycling stability. Additionally, Co_4S_3 , as an active component, is more effective than CoS in suppressing the volume expansion and structural collapse of the material, thereby achieving superior long-cycle performance.

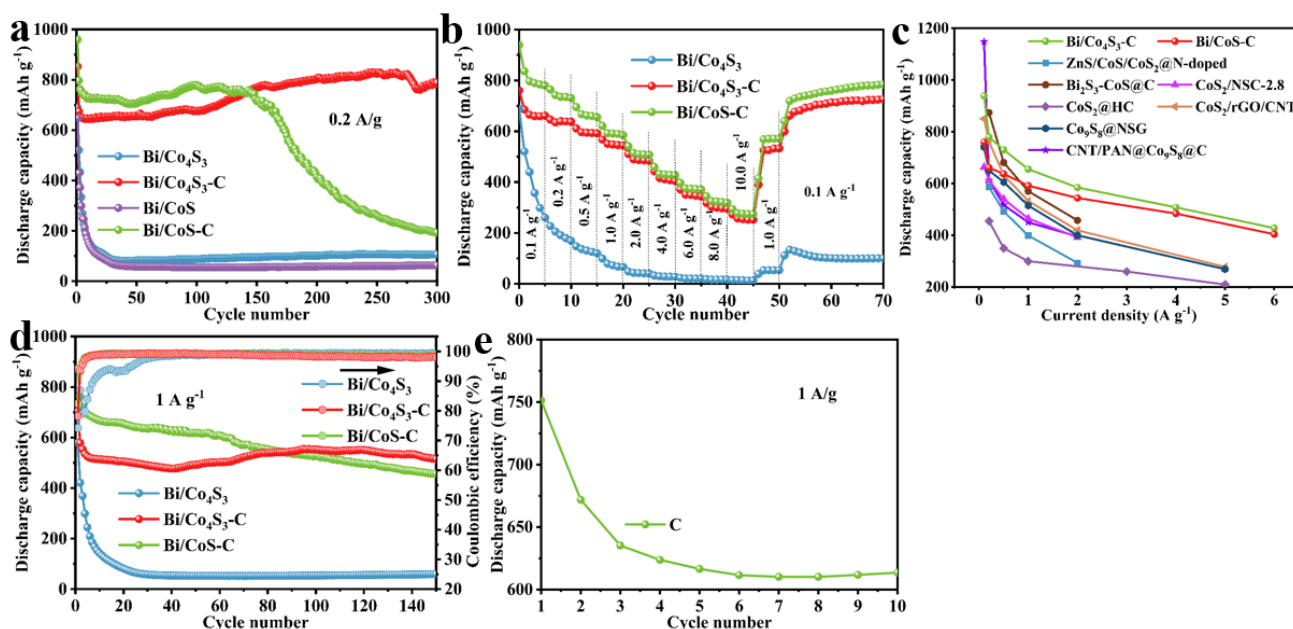


Figure 6. (a) Cycling stability of Bi/CoS, Bi/CoS-C, Bi/Co₄S₃, and Bi/Co₄S₃-C at a current density of 0.2 A/g; (b) Rate performance of Bi/Co₄S₃, Bi/CoS-C, and Bi/Co₄S₃-C; (c) Comparison of rate performance with previously reported literature; (d) Galvanostatic charge-discharge curves of Bi/Co₄S₃, Bi/CoS-C, and Bi/Co₄S₃-C at 1 A/g; (e) Galvanostatic charge/discharge curve of graphite (C) at 1 A/g.

To investigate the charge-discharge capabilities of Bi/CS, Bi/CoS-C, and Bi/CS-C electrodes over a period of time, we conducted rate performance tests, as shown in **Figure 5b**. At current densities of 0.1, 0.2, 0.5, 1, 2, 4, 6, 8, and 10 A/g, the reversible capacities of Bi/CoS-C were 939.2, 779.7, 730.7, 655.6, 584.9, 508.1, 427.9, 371.5, and 319 mAh/g, respectively. In contrast, the reversible capacities of Bi/CS-C were 760.4, 661.4, 637.6, 591.9, 544.4, 484.3, 404.2, 344.1, and 295.4 mAh/g, respectively. It can be observed that the Bi/CoS-C electrode exhibited higher specific capacities at all current densities, indicating its superior rate performance. Further analysis revealed that at a low current density of 0.2 A/g, although Bi/CoS-C exhibited a higher initial capacity, its capacity decayed more rapidly over long

cycles, while the Bi/CS-C electrode showed better cycling stability. This suggests that CoS, as an active component, effectively enhances the rate performance of the material, but its long-term stability still requires optimization compared to the Bi/CS-C electrode. Furthermore, throughout the rate testing, the specific capacities of Bi/CoS-C and Bi/CS-C electrodes were always higher than those of the Bi/CS electrode, indicating that the incorporation of graphite significantly enhanced the rate performance and charge-discharge capabilities of the material. Particularly after high-rate cycling, when the current density was restored to 0.1 A/g, the reversible capacities of the Bi/CoS-C and Bi/CS-C electrodes increased to 719.2 mAh/g and 661.6 mAh/g, respectively, while the reversible capacity of the Bi/CS electrode only increased to 134.2 mAh/g. This further verifies that the incorporation of graphite effectively enhances the structural stability and rate performance of the material. This could be attributed to the high conductivity of graphite and its buffering effect on volume expansion, allowing the electrode to maintain good structural integrity during high-rate charge-discharge cycles, thereby improving cycling life and rate performance. This performance surpasses that of many previously reported cobalt-based sulfide anode materials for LIBs (see **Figure 6c**), demonstrating the significant advantage of the Bi/CoS-C and Bi/CS-C electrodes in terms of rate capability [16,18,25,28,32–34]. To further evaluate the cycling stability of Bi/CS, Bi/CoS-C, and Bi/CS-C electrodes at high current densities, we conducted long-term cycling tests at 1 A/g (as shown in **Figure 6d**). The experimental results showed that the Bi/CS-C electrode maintained a high reversible capacity of 515.4 mAh/g after 150 cycles, demonstrating excellent cycling stability. In contrast, the specific capacity of Bi/CoS-C electrodes exhibited a continuous decrease with increasing cycle numbers, further proving its poor cycling stability, which may be related to the gradual collapse of its structure or loss of active materials during long cycles. In this study, the carbon content and its contribution to the total capacity were estimated based on the designed precursor ratios and independent electrochemical test results. Bi₂S₃ and Co powder were reacted in a molar ratio of 1:4 to produce Bi and Co₄S₃, which were then mixed with exfoliated graphite at a mass ratio of 0.85:0.15 via ball milling to obtain the Bi/CS-C composite. Therefore, the theoretical mass fraction of carbon in the final composite was approximately 15%. Additionally, the exfoliated graphite was independently tested in half-cell configuration, yielding a discharge capacity of approximately 613.6 mAh/g at the 10th cycle, as shown in **Figure 6e**. Based on this, the capacity contribution of the active components in the composite was estimated using the following weighted average formula: Capacity estimation for the Bi/CS-C electrode (taking the 10th cycle as an example), according to Equation (17):

$$C_{total} = w_c \times C_c + w_{active} \times C_{active} \quad (17)$$

$$514.4 = 0.15 \times 613.6 + 0.85 \times C_{active} \rightarrow C_{active} \approx 496.9\text{mAh/g.}$$

Capacity estimation for the Bi/CoS-C electrode:

$$667.5 = 0.15 \times 613.6 + 0.85 \times C_{active} \rightarrow C_{active} \approx 677.0\text{mAh/g.}$$

These results suggest that the majority of the total capacity of the Bi/CS-C electrode originates from the Bi/CS active matrix, while the graphite additive, apart from enhancing structural stability, also provides a modest contribution to capacity. In contrast, although Bi/CoS-C contains the same carbon content, its active components exhibit higher capacity, which is likely attributed to the activation behavior of CoS during the initial cycles and stronger synergistic interactions between CoS and Bi.

To further explore the lithium storage mechanism of Bi/CS-C composites, CV tests were performed at different scan rates, as shown in **Figure 7a**. In the scan rate range of 0.2 to 1.0 mV/s, the peak current increases as the scan rate increases. The relationship between scan rate (v) and peak current (i) can be expressed by Equation (18) [10,35]:

$$\ln i = \ln a + b \ln v \quad (18)$$

a is a constant, and b is the slope, which is related to the ratio of the conversion mechanism and pseudocapacitive behavior. Based on the v and i values at the typical peaks, the b value is calculated (as shown in **Figure 7b**). The results show that the b values of Bi/CS-C electrodes are all greater than 0.65, indicating that their electrochemical behavior is predominantly governed by a capacitive control mechanism. Furthermore, to further compare the pseudocapacitive contributions of Bi/CS, Bi/CS-C, and Bi/CoS-C, CV tests were conducted at different scan rates for these three electrode materials, and the results were analyzed using Equation (19):

$$i = k_1 v + k_2 v^{1/2} \quad (19)$$

In this equation, $k_1 v$ and $k_2 v^{1/2}$ represent the contributions of pseudocapacitive behavior and conversion reactions, respectively. Based on this relationship, the pseudocapacitive contribution ratio was calculated, as shown in **Figure 7c**. Notably, at a scan rate of 1.0 mV/s, the pseudocapacitive contribution of the Bi/CS-C electrode reached 91.6%, while the pseudocapacitive contribution of the Bi/CoS-C electrode was 88.2%, indicating that Bi/CS-C has a more significant pseudocapacitive effect. Moreover, throughout the entire test range, the pseudocapacitive contribution of Bi/CS-C remained above 80%, which is significantly better than the other two electrode materials.

These results strongly demonstrate that the introduction of exfoliated graphite plays a crucial role in enhancing the electrochemical performance of Bi/CS-C and Bi/CoS-C electrodes: (1) Exfoliated graphite provides a rich conductive network, reducing the internal resistance of the electrodes and facilitating fast electron/ion transport; (2) the interlayer structure of graphite provides more active sites for the storage and diffusion of Li^+ , thereby improving the additional capacity; (3) the flexible skeleton structure of exfoliated graphite can effectively buffer the volume expansion of the material during charge/discharge cycles, improving the structural stability and cycle life of the electrodes. The results of this study further confirm that Co_4S_3 , as an active component in Bi/CS-C composites, can effectively enhance the cycling life of the material, showing superior lithium storage performance compared to CoS, and providing important theoretical and experimental support for the development of high-performance LIB anode materials.

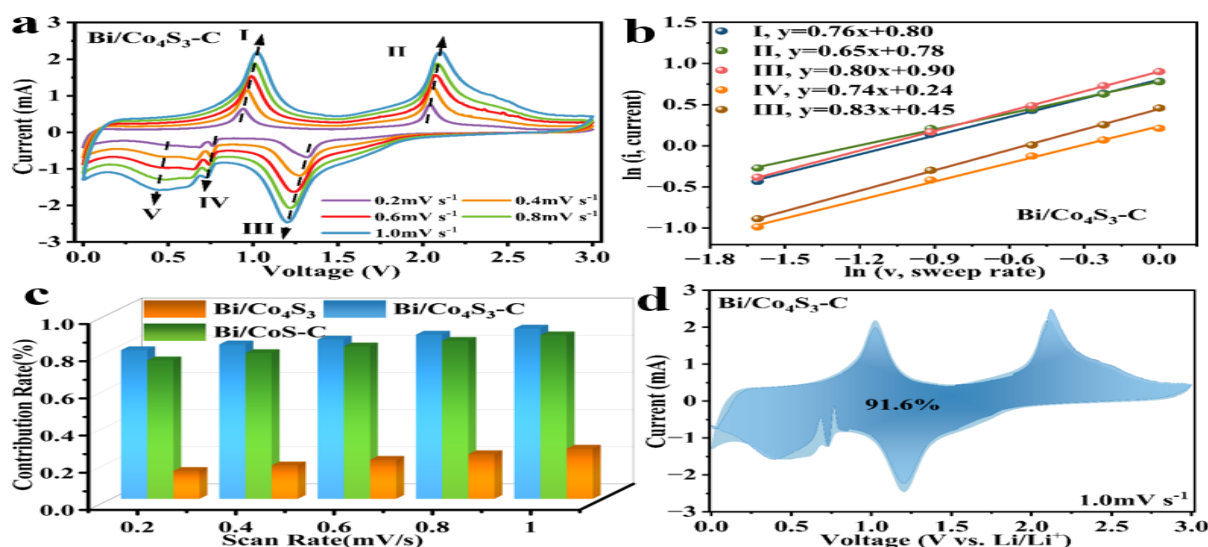


Figure 7. (a) CV curves of Bi/Co₄S₃-C at different scan rates; (b) Determination of the b value based on the sharp peaks of the CV curves of Bi/Co₄S₃-C at different scan rates; (c) Pseudocapacitive contribution ratio of Bi/Co₄S₃, Bi/Co₄S₃-C, and Bi/CoS-C at different scan rates; (d) Surface pseudocapacitance of Bi/Co₄S₃-C at 1.0 mV/s.

4. Conclusion

Guided by theoretical considerations, Bi/CoS-C and Bi/CS-C composites were successfully synthesized via a cost-effective and scalable solid-state ball milling approach. The electrochemical performance of these composites as LIB anodes was systematically evaluated. Ball milling facilitated the homogeneous integration of Bi with CoS or Co₄S₃ and nanoscale graphite, yielding a rough, dense microstructure that enhanced Li⁺ diffusion kinetics and introduced abundant active sites for improved lithium storage. Simultaneously, the lamellar architecture of exfoliated graphite offers abundant reactive sites and constructs a stable conductive network, thereby enhancing cycling stability and rate capability. Moreover, Co₄S₃, as the active component, more effectively suppresses volume expansion and structural degradation compared to CoS, thereby imparting superior long-term cycling stability. Notably, the Bi/CS-C electrode retained a high reversible capacity of 788.8 mAh/g after 300 cycles at 0.2 A/g. In rate capability tests, when the current density was reduced back to 0.1 A/g, the reversible capacities recovered to 719.2 and 661.6 mAh/g for Bi/CoS-C and Bi/CS-C, respectively. This solid-state ball milling strategy offers a low-cost, efficient, and scalable route for the design and optimization of multicomponent transition metal sulfide-based anodes, laying a robust foundation for the development of next-generation high-performance LIBs.

Author contributions: Investigation, TY and LZ; data curation, TY and LZ; formal analysis, LZ; writing—original draft preparation, LZ; writing—review and editing, TZ, and YD; supervision, TZ; project administration, HJ; funding acquisition, TZ and YD. All authors have read and agreed to the published version of the manuscript.

Funding: This work was supported by the Natural Science Foundation of China Youth Program (22405042), and the National Natural Science Foundation of China (22073069 and 21773082).

Institutional review board statement: Not applicable.

Informed consent statement: Not applicable.

Data availability statement: Applicable for reasonable request.

Conflict of interest: The authors declare no conflict of interest.

References

1. Navia Simon D, Diaz Anadon L. Power price stability and the insurance value of renewable technologies. *Nature Energy* 2025. 10(3): 329–341. doi: 10.1038/s41560-025-01704-0
2. Kan X, Reichenberg L, Hedenus F, Daniels D. Renewable export cost index as an indicator of global renewable energy trade potential. *Communications Earth & Environment*. 2025; 6(1): 112. doi: 10.1038/s43247-025-02094-7
3. Costa CM, Pinto RS, Serra JP, et al. Next generation sustainable lithium-ion batteries: Micro and nanostructured materials and processes. *Chemical Engineering Journal*. 2025; 509: 161337. doi: 10.1016/j.cej.2025.161337
4. Jeong H, Kim J, Lee S-H, et al. Iron-catalyzed graphitization of lignocellulose: A pathway to develop artificial graphite as anode materials for lithium-ion batteries applications. *Journal of Alloys and Compounds*. 2025; 1020: 179485. doi: 10.1016/j.jallcom.2025.179485
5. Li X, Deng C, Liu M, et al. Reutilization and upcycling of spent graphite for sustainable lithium-ion batteries: Progress and perspectives. *eScience*. 2025; in press.
6. Wang K, Hua W, Huang X, et al. Synergy of cations in high entropy oxide lithium ion battery anode. *Nature Communications*. 2023; 14 (1): 1487. doi: 10.1038/s41467-023-37034-6
7. Ali S, Bakhtiar SUH, Ismail A, et al. Transition metal sulfides: From design strategies to environmental and energy-related applications. *Coordination Chemistry Reviews*. 2025; 523: 216237. doi: 10.1016/j.ccr.2024.216237
8. Hu X, Ma P, Zhang Z, et al. Emerging transition metal sulfide/MXene composites for the application of electrochemical energy storage. *Chemical Engineering Journal*. 2024; 499: 156272. doi: 10.1016/j.cej.2024.156272
9. Wang S, Qu C, Wen J, et al. Progress of transition metal sulfides used as lithium-ion battery anodes. *Materials Chemistry Frontiers*. 2023; 7(14): 2779–2808. doi: 10.1039/D2QM01200F
10. Jiang S, Mao M, Pang M, et al. N-doped 3D reduced graphene oxide supported C-encapsulated $\text{Co}_9\text{S}_8/\text{Co}_4\text{S}_3$ composites as anode for improved lithium storage. *Journal of Alloys and Compounds*. 2023; 968: 172206. doi: 10.1016/j.jallcom.2023.172206
11. Pantrangi M, Ashalley E, Hafiz W, et al. Core-shell transition metal disulfide grafted carbon matrix composite as an anode material for high-performance lithium-ion batteries. *Journal of Energy Storage*. 2025; 114: 115878. doi: 10.1016/j.est.2025.115878
12. Zheng J, He C, Li X, et al. $\text{CoS}_2\text{-MnS@Carbon}$ nanoparticles derived from metal–organic framework as a promising anode for lithium-ion batteries. *Journal of Alloys and Compounds*. 2021; 854: 157315. doi: 10.1016/j.jallcom.2020.157315
13. Lin Y, Qiu Z, Li D, et al. $\text{NiS}_2\text{@CoS}_2$ nanocrystals encapsulated in N-doped carbon nanocubes for high performance lithium/sodium ion batteries. *Energy Storage Materials* 2018; 11: 67–74. doi: 10.1016/j.ensm.2017.06.001
14. Li ZA, Wang SG, Chen PP, et al. Interface Engineering of MOF-Derived $\text{Co}_3\text{O}_4\text{@CNT}$ and $\text{CoS}_2\text{@CNT}$ Anodes with Long Cycle Life and High-Rate Properties in Lithium/Sodium-Ion Batteries. *ACS Applied Materials & Interfaces*. 2024; 16: 19730–19741. doi: 10.1021/acsami.3c19361
15. Liu M, Wang L, Zeng X, et al. Hierarchical $\text{Ni}_3\text{S}_2/\text{CoS}_2$ Nanosheet Arrays on Ni Foam as Superior Anode Materials for Lithium-Ion Batteries. *ACS Applied Nano Materials*. 2025; 8(14). doi: 10.1021/acsanm.5c00388
16. Lee HR, Kim YS, Lee SY, et al. Bifunctional effects of nitrogen-doped carbon quantum dots on $\text{CoS}_2/\text{mesoporous carbon}$ composites for high-performance lithium-ion batteries. *Applied Surface Science*. 2024; 664: 160228. doi: 10.1016/j.apsusc.2024.160228
17. Shi M, Wang Q, Hao J, et al. MOF-derived hollow $\text{Co}_4\text{S}_3/\text{C}$ nanosheet arrays grown on carbon cloth as the anode for high-performance Li-ion batteries. *Dalton Transactions*. 2020; 49(40): 14115–14122. doi: 10.1039/D0DT03070H
18. Zhou C, Ma X, Liu G, et al. Three-dimensional interwoven $\text{CoS}_2/\text{reduced graphene oxide/carbon nanotubes}$ composite as anode materials for high-performance lithium-ion batteries. *Journal of Alloys and Compounds*. 2024; 972: 172800. doi: 10.1016/j.jallcom.2023.172800

19. Wu J, Wang K, Hu J, et al. Multi-walled Bi₂O₃/Bi@C particles as a high-performance anode material for lithium-ion batteries. *Journal of Energy Storage*. 2024; 102: 114024. doi: 10.1016/j.est.2024.114024
20. Liu X, Xie J, Tang Y, et al. Bi@C sandwiched carbon nanolayers enables remarkable cyclability at high current density for lithium-ion batteries. *Applied Surface Science*. 2023; 613: 155996. doi: 10.1016/j.apsusc.2022.155996
21. Li C, Yang D, Jiang Z, et al. Novel crystalline Bi/amorphous Bi₂O₃ hybrid nanoparticles embedded in N-doped carbon for high-performance lithium-ion battery anodes. *Journal of Physics and Chemistry of Solids*. 2025; 196: 112330. doi: 10.1016/j.jpcs.2024.112330
22. Yu M, Dong Z, Mu J, et al. Fabrication of permselective interlayer with uniform pore structure and in-situ sulfurized Co₄S₃ for high performance lithium sulfur battery. *Separation and Purification Technology*. 2024; 341: 126664. doi: 10.1016/j.seppur.2024.126664
23. Jiang M, Hu Y, Mao B, et al. Strain-regulated Gibbs free energy enables reversible redox chemistry of chalcogenides for sodium ion batteries. *Nature Communications*. 2022; 13(1): 5588. doi: 10.1038/s41467-022-33329-2
24. Hu Y, Li H, Gu H, et al. Al³⁺ pre-intercalation and g-C₃N₄ coating synergistically modulate gibbs free energy for robust and compatible MnO₂ cathodes in aqueous aluminum batteries. *Chemical Engineering Journal*. 2025; 507: 160532. doi: 10.1016/j.cej.2025.160532
25. Chen X, Wang P, Zhang Z, Yin L. Bi₂S₃-CoS@C core-shell structure derived from ZIF-67 as anodes for high performance lithium-ion batteries. *Journal of Alloys and Compounds*. 2020; 844: 156008. doi: 10.1016/j.jallcom.2020.156008
26. Wang H, Ma J, Liu S, et al. CoS/CNTs hybrid structure for improved performance lithium ion battery. *Journal of Alloys and Compounds*. 2016; 676: 551–556. doi: 10.1016/j.jallcom.2016.03.132
27. Chen Y, Lu C, Yuan S, et al. N-doped carbon nanotubes and CoS@NC composites as a multifunctional separator modifier for advanced lithium-sulfur batteries. *Journal of Colloid and Interface Science*. 2025; 680: 405–417. doi: 10.1016/j.jcis.2024.11.108
28. Cheng W, Di H, Shi Z, et al. Synthesis of ZnS/CoS/CoS₂@N-doped carbon nanoparticles derived from metal-organic frameworks via spray pyrolysis as anode for lithium-ion battery. *Journal of Alloys and Compounds*. 2020; 831: 154607. doi: 10.1016/j.jallcom.2020.154607
29. Dong C, Guo L, Li H, et al. Rational fabrication of CoS₂/Co₄S₃@N-doped carbon microspheres as excellent cycling performance anode for half/full sodium ion batteries. *Energy Storage Materials*. 2020; 25: 679–686. doi: 10.1016/j.ensm.2019.09.019.
30. Cao Y, Zhou X, Gao F. Reconfiguration of metal-organic frameworks to form ultrafine Bi dots as an excellent high-current performance of lithium-ion battery anode. *Journal of Alloys and Compounds*. 2024; 992: 174650. doi: 10.1016/j.jallcom.2024.174650.
31. Fu H, Shi C, Nie J, et al. Bi₂O₃ nanospheres coated in electrospun carbon spheres derived Bi@C used as anode materials for lithium-ion batteries. *Journal of Alloys and Compounds*. 2022; 918: 165666. doi: 10.1016/j.jallcom.2022.165666
32. Wang Z, Qi J, Han L, et al. CoS₂ nanoparticles embedded in N-doped hollow carbon nanotubes as anode materials for high performance lithium-ion battery. *Materials Letters*. 2024; 364: 136332. doi: 10.1016/j.matlet.2024.136332
33. Li Y, Bao Y, Han B, et al. 3D-structured Co₉S₈@NSG prepared using deep eutectic solvents as high-performance anode material of lithium-ion batteries. *FlatChem*. 2024; 45: 100635. doi: 10.1016/j.flatc.2024.100635
34. Gao J, Wang X, Huang Y, et al. Hollow core-shell structured CNT/PAN@Co₉S₈@C coaxial nanocables as high-performance anode material for lithium ion batteries. *Journal of Alloys and Compounds*. 2021; 853: 157354. doi: 10.1016/j.jallcom.2020.157354
35. Chen Q, Hu J, Xia Q, Zhang L. Complexation-assisted polymerization for the synthesis of functional silicon oxycarbonitride with well-dispersed ultrafine CoS as high-performance anode for lithium-ion batteries. *Journal of Alloys and Compounds*. 2023; 949: 169824. doi: 10.1016/j.jallcom.2023.169824